

ISTANBUL TECHNICAL UNIVERSITY ★ GRADUATE SCHOOL OF SCIENCE
ENGINEERING AND TECHNOLOGY

**COMPARISON OF ALGEBRAIC RECONSTRUCTION ALGORITHMS FOR
TOMOSYNTHESIS**

M.Sc. THESIS

Kübra CENGİZ

Department of Computer Engineering

Computer Engineering Programme

JANUARY 2014

ISTANBUL TECHNICAL UNIVERSITY ★ GRADUATE SCHOOL OF SCIENCE
ENGINEERING AND TECHNOLOGY

**COMPARISON OF ALGEBRAIC RECONSTRUCTION ALGORITHMS FOR
TOMOSYNTHESIS**

M.Sc. THESIS

Kübra CENGİZ
(504111518)

Department of Computer Engineering

Computer Engineering Programme

Thesis Advisor: Assoc. Prof. Dr. Mustafa Ersel KAMAŞAK

JANUARY 2014

İSTANBUL TEKNİK ÜNİVERSİTESİ ★ FEN BİLİMLERİ ENSTİTÜSÜ

**TOMOSENTEZ İÇİN CEBİRSEL GERİ ÇATMA ALGORİTMALARININ
KARŞILAŞTIRILMASI**

YÜKSEK LİSANS TEZİ

**Kübra CENGİZ
(504111518)**

Bilgisayar Mühendisliği Anabilim Dalı

Bilgisayar Mühendisliği Programı

Tez Danışmanı: Doç. Dr. Mustafa Ersel KAMAŞAK

OCAK 2014

Kübra Cengiz, a M.Sc student of ITU **Graduate School of Science and Engineering and Technology** student ID **504111518**, successfully defended the thesis entitled “**COMPARISON OF ALGEBRAIC RECONSTRUCTION ALGORITHMS FOR TOMOSYNTHESIS**”, which she prepared after fulfilling the requirements specified in the associated legislations, before the jury whose signatures are below.

Thesis Advisor : **Assoc. Prof. Dr. Mustafa KAMAŞAK**
İstanbul Technical University

Jury Members : **Prof. Dr. Mustafa ÖZATEŞ**
Nişantaşı University

Assoc. Prof. Dr. Hazım Kemal EKENEL
İstanbul Technical University

Date of Submission : 22 September 2009

Date of Defense : 21 December 2009

To my family,

FOREWORD

First of all, I want to thank my supervisor Assoc. Prof. Dr. Mustafa E. Kamaşak of being great help during the development of this thesis.

Secondly, I thank Assis. Prof. Dr. İsa Yildirim who made contributions on improving my results and I am very grateful to Prof. Dr. Oğuz Dicle for his ideas and guidance.

And lastly, I like to give my special thanks to my extended family for their neverending support and encouragement.

January 2014

Kübra CENGİZ

Computer Engineer

TABLE OF CONTENTS

	<u>Page</u>
FOREWORD	ix
TABLE OF CONTENTS	xi
ABBREVIATIONS	xiii
LIST OF TABLES	xv
LIST OF FIGURES	xvii
SUMMARY	xix
ÖZET	xxi
1. INTRODUCTION	1
1.1 Breast Cancer	1
1.2 Mammography	2
1.3 Digital Mammography	2
1.4 Breast CT.....	3
1.5 Digital Breast Tomosynthesis	4
1.6 Hypothesis	8
2. METHODS	9
2.1 Siddon's Algorithm	9
2.2 Algebraic Reconstruction Technique	12
2.3 Multiplicative Algebraic Reconstruction Technique	14
3. RESULTS	17
3.1 Results of Phantom I	20
3.2 Results of Phantom II	23
4. DISCUSSION	27
5. CONCLUSIONS	29
REFERENCES	31
CURRICULUM VITAE	37

ABBREVIATIONS

SFM	: Screen-film mammography
DM	: Digital mammography
CAD	: Computer aided detection/diagnosis
CT	: Computed tomography
2D	: Two-dimensional
3D	: Three-dimensional
MITS	: Matrix inversion tomosynthesis
FB	: Filtered back projection
ART	: Algebraic reconstruction techniques
MART	: Multiplicative algebraic reconstruction techniques
RMSE	: Root mean square error
SSIM	: Structural similarity
MSSIM	: Mean structural similarity
LOI	: Layer of interest
CNR	: Contrast-to-noise-ratio
FFDM	: Full-field digital mammography
ROC	: Receiver operating characteristic

LIST OF TABLES

	<u>Page</u>
Table 3.1 : Phantoms parameters.	18
Table 3.2 : MART parameters	18

LIST OF FIGURES

	<u>Page</u>
Figure 1.1 : Age-specific female breast cancer incidence (2004-2008) mortality(2003-2007) rates.	1
Figure 1.2 : The signal on the image receptor with conventional mammography depends on the total attenuation of all the tissue.	6
Figure 1.3 : Tomosynthesis imaging obtains the images from different angles separating structures at differing heights.	7
Figure 2.1 : Geometric illustration of a ray on image grid.	9
Figure 3.1 : LOI image of phantom I.....	19
Figure 3.2 : LOI image of phantom II.....	19
Figure 3.3 : Images of the LOI (29 th layer of the phantom) upper row from left to right shows reconstructed LOI image using MART (p= 0.5, method I), using MART (p= 1, method I), and bottom row from left to right shows using MART (method II), using ART grid.....	21
Figure 3.4 : RMSE value comparison of MART (p=0.5,method I), (p=1,method I), (method II), and ART for phantom I.....	22
Figure 3.5 : MSSIM value comparison of MART (p=0.5,method I), (p=1,method I), (method II), and ART for phantom I.....	22
Figure 3.6 : Images of the LOI (11 th layer of the phantom) upper row from left to right shows reconstructed LOI image using MART (p=0.5, method I), MART (p=1, method I), and bottom row from left to right shows using MART (method II) using ART.....	23
Figure 3.7 : RMSE value comparison of MART (p=0.5,method I), (p=1,method I), (method II), and ART for phantom II ...	24
Figure 3.8 : CNR value comparison of MART (p=0.5,method I), (p=1,method I), (method II), and ART for phantom II... ..	25
Figure 3.9 : MSSIM value comparison of MART (p=0.5,method I), (p=1,method I), (method II), and ART for phantom II... ..	25

COMPARISON OF ALGEBRAIC RECONSTRUCTION ALGORITHMS FOR TOMOSYNTHESIS

SUMMARY

Breast cancer is an extremely important health problem worldwide. It's among the most common form of cancer observed on women. Mammography is a radiographic examination designed to detect breast cancer. Digital mammography has brought many advantages to the diagnosis of breast cancer. Film and digital mammography have equal diagnostic accuracy in screening of breast cancer, but the accuracy of digital mammography is higher in women less than 40 year-old and having dense breasts. Digital mammography develops in accordance with computer technology to produce digital images of the breast. Therefore, it enables to remove physical storage by means of the possibility of electronic transfer and the storage of images. Computed tomography (CT) was used for breast imaging in the beginning. The CT system was not practically used because of poor image quality and taking long scanning time. Furthermore, the entire chest to be scanned is necessary for the use of a body scanner in breast imaging. Therefore, it resulted in increased patient dose and poorer resolution of the reconstructed breast images. Digital Breast Tomosynthesis (DBT) is an innovative 3D imaging technique implemented using a limited number of low dose projections, which are taken with the x-ray source moving in a limited angle of rotation around the breast. Then these low dose projection images should be processed using mathematical methods, to reconstruct tomographic images, resulting in a 3D representation of the imaged breast. In tomosynthesis imaging, out-of-focus slice blur problem arises due to incomplete sampling problem. Several approaches have been suggested to deal with this problem. The purpose of this work is to implement from among these approaches Algebraic Reconstruction Technique (ART) and Multiplicative Algebraic Reconstruction Technique (MART). Former studies generally offered solutions for 2D tomosynthesis image reconstruction problem. In this study, a 3D phantom model was used. All of the algorithms and experiments are programmed with C++. The difference between two reconstruction algorithms is also investigated by means of comparing root mean square error (RMSE), contrast to noise ratio (CNR) value, and mean structural similarity (MSSIM).

TOMOSENTEZ İÇİN CEBİRSEL GERİ ÇATMA ALGORİTMALARININ KARŞILAŞTIRILMASI

ÖZET

Meme kanseri dünya çapında önemli bir sağlık sorunudur. Bayanlar arasında en çok gözlenen kanser çeşididir. Mamografi meme kanserinin tanımlanması için özel tasarlanmış radyografik bir incelemedir. Mamografinin film teknolojisinden sayısal hale geçişi meme kanseri teşhisine bir çok avantaj sağlamıştır. Tümörün erken teşhis rolü sayesinde son on yılda ölüm oranlarında %20 kadar bir düşüş sağlamıştır. Ancak teşhislerde bazı sınırlamaları vardı. Meme kanseri teşhisinde neden olduğu kısıtlamalardan dolayı var olan mamografi teknolojileri ilerletilmiş ve yenileri geliştirilmiştir. Sayısal mamografi (DM), bilgisayar destekli teşhis (CAD), meme tomosentezi, mıknatıslı rezonans görüntüleme (MRI) ve ultrason, umut veren meme görüntüleme yeni teknolojilerinden bazılarıdır.

Meme kanserini görüntüleme açısından sayısal ve film mamografisinin teşhis başarısı aynıdır, ancak sayısal mamografi 40 yaşından daha genç bayanlarda daha başarılıdır. Sayısal mamografi memenin sayısal görüntüsünü sağlamak için bilgisayar teknolojisine göre gelişir. Görüntüler sayısal işaret olarak tutulur, böylece elektronik transferi ve görüntülerin depolanması mümkündür. Bu da filmin gerektirdiği dağıtımı ve fiziksel depolamayı önler. Elektronik kopyalama, bilgisayar destekli teşhis ve üç boyutlu görüntüleme mamografik yorumlamada ilerleme için çok iyi fırsat sunar. Sayısal mamografi önemli derecede düşük dozda radyasyon gösterdiği ve hatırlatma ve biopsi oranlarını düşürdüğü için sayısal mamografiye erişim artmaya devam edecektir. Örneğin Amerikan meme görüntüleme tesislerinin %60 ' tan fazlası sayısal mamografi kullanır ve her yıl daha çok dijital servis elde etmektedirler. Sayısal mamografi sistemleri ekran filmi görüntüleme sistemlerinde, özellikle dinamik aralıklarda görüntüleme, sayısal elde edinimde, depolama, görselleştirme ve son işlemlerde gelişme sağlamıştır. Sayısal mamografi hala hızlı bir şekilde gelişmektedir ve hasta bakımında etkili olacaktır.

Tomosentez, telemamografi, sayısal görüntü işleme ve CAD gibi yeni uygulamalar üzerinde hala devam eden gelişmeler mevcuttur. Telemamografi az hizmet alan yerlerde ve coğrafi açıdan uzak olan popülasyonlarda en son meme bakımına erişimi sağladığı için dijital mamografi ile birlikte çok etkilidir. Mamografi görüntülerinin sayısal formatı sayesinde sayısal görüntü işleme tekniklerinin kullanılabilir. Memedeki farklı yapıların zıtlığına göre yapılan işlemler kanserin belirlenebilirliğini artırabilir. Aynı zamanda, kenar iyileştirme ya da görüntü yumuşatma ve şüpheli alan üzerinde yakınlaştırma gibi görüntü işleme teknikleri daha iyi bir görüntüleme sağlar. Diğer bir uygulama olan bilgisayar destekli teşhis önemli bir araştırma alanıdır. Dijital görüntüler yazılımlar tarafından incelendikten sonra, daha ileri gözlem için radyologlar şüpheli bölgelerin üstünde dururlar. Bu sistemlerin zorluğu hassaslığı ve özgünlüğü arasında uygun bir denge bulmaktır. Özgünlük artarsa

görüntü üzerinde işaretlenmiş çok sayıda yanlış pozitifle sonuçlanır. Aksine doğru pozitifler yeterince işaretlenmezse sistem radyologlara yeteri kadar yardımcı olamaz.

Bilgisayarlı tomografi başlarda meme görüntülemeye kullanılmıştır. Sistemin gelişmesi ve ticari olarak kullanımının artmasıyla vücut görüntülemeye de kullanılmıştır. Düşük görüntüleme kalitesi ve uzun tarama zamanından dolayı bu sistem pratik olarak çok kullanılmamaktadır. Buna ek olarak, bu sistem için meme görüntülemeye bütün göğsün taranması gerekmektedir. Teknolojik kısıtlardan dolayı 2000' lerin başında bu tarama tekniği önemsiz hale gelmiştir. Genel radyografi ve mamografi uygulamaları için çeşitli düz panel ekran detektörler geliştirilmiştir. Bu detektörler, 1990' larda sayısal x-ışın sistemlerini oluşturmak için kullanılmıştır. Detektörlerin akademik birimlerde kullanılabilirliğinin artırılması için bazı algoritmalar geliştirilmiştir. Meme anatomisinin ve yumuşak meme dokularının gösterilmesi ve bulunması açısından bilgisayarlı meme tomografi görüntülerinin mamogramdan daha çok tercih edilmesi için güncel hasta çalışmaları yapılmıştır. Ancak, bu görüntüler küçük kireçlenmelerin gösteriminde kısıtlı kalmıştır. Yinelemeli algoritmalar, son zamanlarda x-ışın dozunda azalma sağlamış olmalarına rağmen, bu algoritmalar genellikle geri çatmayı tamamlamak için çok zaman harcarlar.

Tomosentez 3 boyutlu mamografinin bir uygulanma türüdür. X-ışın dozu neredeyse geleneksel 2 boyutlu mamografi ile aynıdır. Tomosentez görüntüleme göğüs, eklem, diş ve meme görüntüleme gibi birçok uygulamada araştırma alanına sahiptir. Bu konu üzerinde araştırmacı ve üretici firma birçok araştırma ve çalışma yapılmıştır, yeni teknikler geliştirilmiştir. Çoğu üretici firma aleni satış için ticari tomosentez cihazı sağlamada aktif rol oynamaktadır. Birçok meme tomosentez tarayıcıları GE, Hologic, Siemens ve Philips gibi ticari satıcılar tarafından sağlanmaktadır. Anatomik yapının üst üste gelerek oluşturduğu nesnelere ayırt edilmesi için geliştirilen 3 boyutlu görüntüleme teknikleri girişimleri 20. yüzyılın başlarına dayanır.

Radon, 2 boyutlu izdüşüm verisinden nesnenin düzlemlerini oluşturmayı matematiksel olarak tanımladı. Ziednes des Plantes de geleneksel doğrusal tomografi üzerine çalışmalar yaptı ve Ernest Twining de klinik denemeler yaptı. Başlangıçta tomografi sisteminde, bir odak noktası oluşturmak için film algılayıcısı ve x-ışın tüpünün doğrusal bir hareketi gerekliydi. Birden fazla odak noktası istenirse bu işlem tekrarlanacaktır. Bu da hastaların yüksek dozda radyasyona maruz kalmasına neden olacaktır. Diğer bir dezavantaj ise odak dışı dilim bulnaklığı yeterli bir şekilde önlenemez. Sayısal x-ışın elde edilecek teknolojilerinde ilerlemeler sayesinde 1990 ların başında bir dizi izdüşüm görüntüsü memenin derinliğini elde etmek için farklı açılardan alınarak elde edilmiştir.

Son zamanların meme tomosentez tarayıcılarının tasarımları tam alan sayısal mamografi sistemi temellidir ve birbirlerine çok benzerler. Geleneksel x-ışın tüpü sıkıştırılmış meme üzerinde sınırlı izomerkezsel bir dönme hareketi yaparak sınırlı açıda bir dizi izdüşüm görüntüleri elde eder. İzlenen bu yol detektöre paraleldir. X-ışın tüpünün dönme merkezi göz önüne alınarak otomatik olarak döndüğünden emin olabilmek için mekanik tasarım, yazılım ve tam bir açı ölçen cihaz kullanılır. Aynı zamanda her bir izdüşüm görüntüsü için x-ışın tüpünün açısal olarak tam konumunun kaydedilmesi gereklidir. Tipik bir tomosentez taraması yaklaşık 20 saniye sürer. Bu süre bakış açısı sayısına bağlıdır. Son zamanlarda Amerikan gıda ve ilaç kurumu sadece bir meme tomosentez cihazının ticaretini onaylanmıştır, o da ilk teşhiş

ürünlerinin lider üreticilerinden biri olan Hologic tarafından yapılmış Selenia Dimensions'dır.

Dijital tomosentez meme görüntüleme ve teşhis sisteminin yeni bir türüdür. Her bir memenin çoklu x-ışın görüntüleri farklı açılardan alınarak elde edilir. Meme, geleneksel mamografideki gibi konumlanır, ama sadece çok küçük bir baskı uygulanır. Bu baskı, işlem boyunca memenin sabit bir pozisyonda tutulmasını sağlayacak kadardır. X- ışın tüpü meme etrafında yay çizer ve meme ile ilgili odaklanmış 3 boyutlu görüntüleri net bir şekilde elde etmek için işlem boyunca alınan bilgiler bilgisayara gönderilir. Bu çalışma görüntüleme mamografideki dozla başarılabilir. Projeksiyon görüntülerinde tomografik görüntülerin geriçatılması için matematiksel yöntemler kullanılarak memenin üç boyutlu görüntüsü elde edilir.

İleri izdüşüm almak için Siddon' nun algoritması kullanılır. Işın x-ışın tüpünden çıkıp görüntü dizilerinde yol izlerken 3 boyutlu nesnenin içinden geçtiği uzunluğu hesaplamada hızlı ve doğru bir algoritmadır. Elde edilen izdüşüm görüntülerinin geriçatılması için kullanılan tekniklerden biri de Cebirsel Geriçatma Tekniğidir. İlk olarak Kaczmarz tarafından tasarlanmıştır. Daha sonra Gordon ve arkadaşları bu tekniği görüntülerin geri çatılmasında kullanmıştır. Bu teknik, istenilen nesneyi geri çatmak için izdüşüm görüntüleri kullanarak satırlar üzerinde bir çalışan bir algoritmadır. Ayrıca, sınırlı açıda geri çatma problemine alternatif bir çözümdür. Asimetric nesnelere kolayca çalışabilir ve sınırlı açıda detaylar üretebilir. Diğer bir geri çatma tekniği de Çarpımsal Cebirsel Geriçatma Tekniğidir. CT görüntülerinin geri çatılmasında doğrusal olmayan yinelemeli bir algoritmadır. Formülündeki üssel değişken olan gevşetme katsayısı için çeşitli öneriler bulunmaktadır. Bu algoritma, karanlık arka plandaki yüksek zıtlıklı nesnelere tomografik geri çatma problemine bir çözüm sağlayabilir. Diğer algoritmalarla karşılaştırıldığında, bu teknik öncesinde bahsedilen problem tarzına daha iyi bir sonuç verir. Bu teknik, diğer algoritmalarla karşılaştırıldığında az yineleme ile daha iyi geri çatma kalitesine sahip olmasına rağmen daha uzun hesaplama zamanı alır ve daha çok hafıza kaplar.

Tomosentez görüntülerinde, tamamlanmamış örnekleme probleminden dolayı odak dışı dilim bulanıklığını oluşturmaktadır. Bu problemin çözümü için birçok yaklaşım mevcuttur. Bu çalışmanın amacı bu yaklaşımlardan olan Cebirsel Geriçatma Tekniği ve Çarpımsal Cebirsel Geriçatma Tekniği gerçekleştirmektir. Önceki çalışmalar genellikle iki boyutlu tomosentez görüntülerinde geriçatma problemine çözüm getirmişlerdir. Bu çalışmada ise üç boyutlu fantom modeli kullanılmıştır. Tüm algoritmalar ve deneyler C++ ile programlanmış ve gerçekleştirilmiştir. Ele alınan iki geriçatma algoritması arasındaki fark ortalama karesel hata ve zıtlık gürültü oranı değerlerinin karşılaştırılmasıyla bulunur.

1. INTRODUCTION

1.1 Breast Cancer

Breast cancer is one of the most common form of cancer among females. The mortality rate of breast cancer takes the second place after lung cancer in the U.S, but especially for women, with an age range 40-55, breast cancer is the leading cause of death. In 2005, almost 40,410 women died of breast cancer [2]. In U.S. the incidence and mortality rate of breast cancer generally raise in parallel with age 95% of new cases and 97% of deaths from breast cancer in 40 year-old women as shown Figure 1.1 [1].

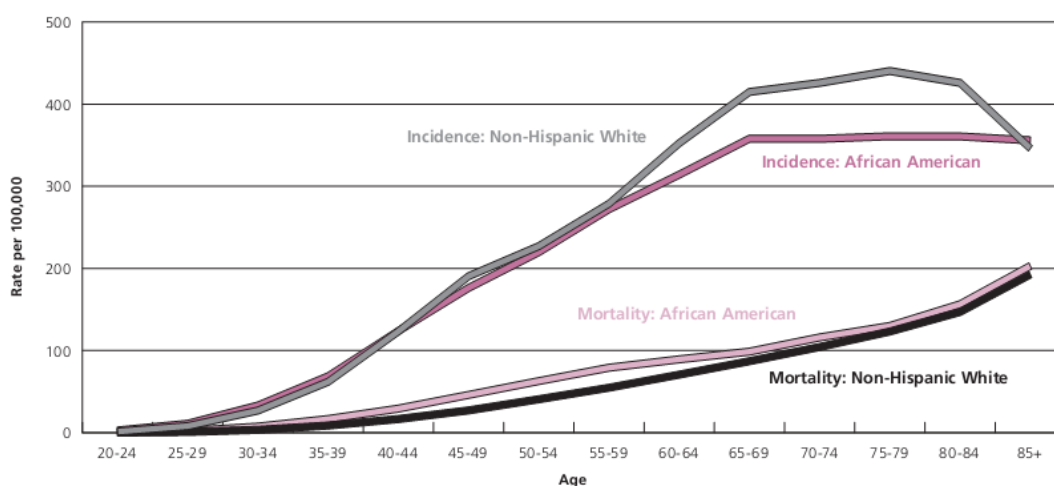


Figure 1.1: Female breast cancer incidence according to ages and (2004-2008) mortality rates (2003-2007) [1].

Since the causes of breast cancer are not completely known, early diagnosis is required in decreasing the death rate. Mammography is the most effective method for early detection of breast cancer at this time [3, 4], and microcalcifications, which are tiny calcium deposits appearing on the mammograms as bright spots, are important signal of early stage of breast cancer [5].

1.2 Mammography

Mammography is a radiographic examination designed to detect breast cancer. Mammography played a vital role in decreasing the death rate by 20% via early tumor detection in the last decade. Although mammography is determined as the most effective method for early detection of breast cancer, the modality has the limitations. It has 20% false-negative rates, where the modality fails to detect cancers and 12% false-positive rates, which is noticed a cancer though there is none. Moreover, though it detects almost 90% of tumors in women over the age of 50, it can detect only 60% of tumors in women under the age of 50 because of dense breast tissue. The other limitation is that the modality lacks of specificity, where mammography cannot identify between malignant and benign breast lesions. Due to these limitations of mammography, new solutions and technologies in breast imaging including computer-aided detection (CAD), digital mammography (DM), and breast tomosynthesis have been proposed [2].

1.3 Digital Mammography

Digital mammography is currently the most effective diagnostic and screening device for early detection of breast cancer. Film and digital mammography have equal diagnostic accuracy in screening of breast cancer, but the accuracy of digital mammography is higher in women less than 40 year-old and having dense breasts [26].

Flat panel x-ray detectors can present very high quantum efficiency and high resolution. These digital detectors allow reducing dose while improving image quality, and therefore, help the development of new imaging techniques like tomosynthesis. Furthermore, the essential detector properties of digital mammography are geometrical characteristics, quantum efficiency, sensitivity, spatial resolution, noise characteristics, dynamic range, uniformity, and acquisition speed. The rate where sequential images obtained is also crucial for dynamic studies such as tomosynthesis.

Digital mammography develops in accordance with computer technology to produce digital images of the breast. Therefore, it enables to remove physical storage by means of the possibility of electronic transfer and the storage of images. Digital

systems offer a wide dynamic variety of operation and a successful visualization of the breast. For optimizing contrast for each imaging task, the digital format allows gray scale adjustment. Additionally, Computer-aided diagnosis, three-dimensional imaging, and softcopy reading provide great opportunities for advancement in mammographic interpretation [6].

In mammography, image quality depends on the shape, the dimensions, and the anatomic structure related to x-ray absorption of region to be scanned. In addition, x-ray beam quality, the resolution, and the noise properties of the imaging system are important [27].

As digital mammography has indicated significantly lower radiation dose and reduced the recall and biopsy rates, accessing to digital mammography will likely continue to increase. More than 60% of U.S. companies on breast imaging provide digital mammography and are acquiring more digital services every year. Also, digital mammography systems suggest improvements on screen film imaging systems, particularly in imaging dynamic range, digital acquisition, storage, display and post processing. Digital mammography is still improving rapidly and will mean more effective and efficient patient care [6].

1.4 Breast CT

Computed tomography (CT) was used for breast imaging in the beginning. After computed tomography (CT) was developed and commercialized and involved the use of a specially designed CT system [28-31] as well as a conventional body scanner [33,34], the efforts to develop breast CT (BCT) began. Because image quality was poor and it took long scanning time, the CT system was not practically used. Furthermore, the entire chest to be scanned is necessary for the use of a body scanner in breast imaging. Therefore, it resulted in increased patient dose and poorer resolution of the reconstructed breast images. The notion of a devoted BCT scanner was unimportant until the early 2000s because of technological limitations.

Several flat panel detectors were developed for general radiography as well as mammography applications; and they were used to construct digital x-ray systems in the 1990s. Cone beam computed tomography (CBCT) techniques were developed with the availability of these detectors in academic institutions. Boone et al. at the University of California and Davis and Ning et al. at the University of Rochester

independently used CBCT techniques for BCT [35-40]. For clinical evaluation, the first patient imager was generated by the former. The latter's efforts led to commercialize the BCT technology. Patient studies conducted up-to-date have indicated that BCT images are preferable to mammography in terms of finding and displaying breast anatomy and soft tissue masses. However, the images are more restricted in visualizing small micro calcifications. Although iterative algorithms have recently been shown to have the potential advantage of dose reduction, they generally take much longer time to complete the reconstruction [6].

1.5 Digital Breast Tomosynthesis

Attempts for developing three-dimensional imaging methods to discriminate objects from overlying anatomical structure date back to the early 20th century [41]. In 1917, Radon suggested the famous Radon transformation of tomography. He described the mathematics of generating internal object planes from two-dimensional projection data [42]. In 1932, Ziedses des Plantes led to study the conventional linear tomography and Ernest Twining launched the clinical trials [41,43]. Early tomography systems required a linear, against motion of the x-ray tube and the film receptor to generate a focal plane. If more than one focal plane was needed, the process had to be repeated. As a result, this led to give high dose to the patients. Secondly, suppressing out-of-plane blur is not sufficiently prevented in this modality [41]. In the late 1990s, a sequence of projection images are obtained from different views to be retained the depth of breast due to the improvement of digital x-ray acquisition technology [41,44].

Tomosynthesis is a type of implementing 3D mammography. Its doses are identical to conventional 2D x-ray mammography. Tomosynthesis imaging has already been researched on many applications such as chest imaging, joint imaging, angiography, dental imaging, and breast imaging [45-60]. A few researches and studies have been made by several research groups and manufacturers. For instance, in 1997 Niklason and colleagues published a tomosynthesis method with the x-ray tube moved in an arc above the stationary breast and detector [61]. Also, in 2003 Wu et al. has a report about the maximum likelihood iterative algorithm (MLEM) to reconstruct the three-dimensional distribution of x-ray attenuation in the breast [62], matrix inversion tomosynthesis (MITS) technique in breast

tomosynthesis [63], filtered back-projection (FBP) [45,64-69], algebraic reconstruction techniques (ART) [49], etc. Major manufacturers are actively involved in providing commercial tomosynthesis devices for public sale. Several prototype breast tomosynthesis scanners have been produced by commercial sellers such as GE, Hologic and Siemens. They have been investigated by several research groups [49,60,62,70,71].

Substantial effort has been made to improve breast tomosynthesis systems by different research groups and companies. Recently, different techniques have been designed and performed manually and automatically to implement and optimize imaging configurations and image reconstruction algorithms, as well as to help identify the best tomosynthesis acquisition strategy.

The designs of most up-to-date breast tomosynthesis scanners are based on a full-field digital mammography (FFDM) system, and are similar to each other. A conventional x-ray tube mounted on a rotating arm drifts an arc above the compressed breast with a partial isocentric motion to generate a series of projection images with the limited angle. The path of the x-ray tube is located on the plane which is parallel to the detector plane. To ensure that the x-ray tube rotates automatically with regard to the rotation center, mechanical design, related control software, and an accurate angle measurement device are used. Also, they are necessary to record exactly angular location of the x-ray tube for each projection view. A typical tomosynthesis scan takes approximately 20 seconds. The time depends on the number of views acquired. Recently, the U.S. Food and Drug Administration approved the commercialization of a breast tomosynthesis device, Selenia Dimensions made by Hologic, Inc., one of the leading manufacturers of premium diagnostic products. This system upgrades the full-field digital mammography (FFDM) system to provide the rotation of x-ray tube along an arc above the digital detector [6].

Tomosynthesis acquires a series of images obtained from projecting a compressed breast at different angles during a limited scan. The images are reconstructed into a 3D series of slices. Considering a total dose required for standard screening mammography, the individual slices decrease structural noise and tissue overlap related to standard 2D projection mammography. Advantages of the digital tomosynthesis device are the reduced breast compression, improved 3D lesion

localization, diagnostic and screening accuracy, and contrast enhanced 3D imaging. In Figure 1.2, the two objects independently attenuate x-rays passing through them on the way to the detector, but the detected signal shows their total attenuation. In mammography, which is a 2D imaging modality, lesions of interest are more difficult to represent due to the mess of signals from objects above and below. Tomosynthesis can decrease this tissue overlap effect because of 3D imaging method.

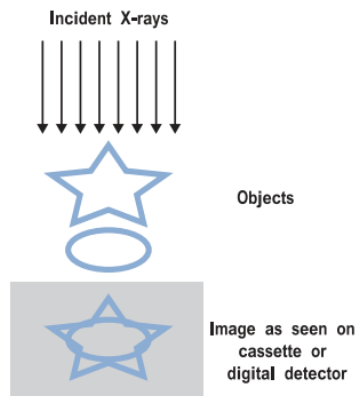


Figure 1.2: The signal on the detector with mammography depends on the summation of attenuation of all the tissues [2].

The logic behind tomosynthesis acquisition theory is shown in Figure 1.3. While the breast is held, several images are obtained at different angles. In Figure 1.3, the objects at different heights in the body like breast tissues are projected in the different views. Although the two objects (ellipse and star) are added up when the x-ray tube is at 0° in this example, acquisitions between $+15^\circ$ and -15° displace the shadows of the objects related to one another in the projections. However, conventional mammography acquires only the central image.

In the tomosynthesis procedure the final step is the reconstruction of the data to obtain 3D information. In Figure 1.3, on the right side of the figure, after the projection images are summed, shifting one related to another in a specific way reinforces the ellipsoidal object and reduces the contrast of the starred object by blurring it out. Also, on the left side of the figure, the same objects can be reconstructed by using different shifts of the projection data in order to reinforce the star object and blur the ellipse. The images are generated by using appropriate shifting of the projections in this method. The reconstruction process computes high-

resolution images whose planes are parallel to the breast support in spite of at a lower dose, and if desired, these can be viewed as well.

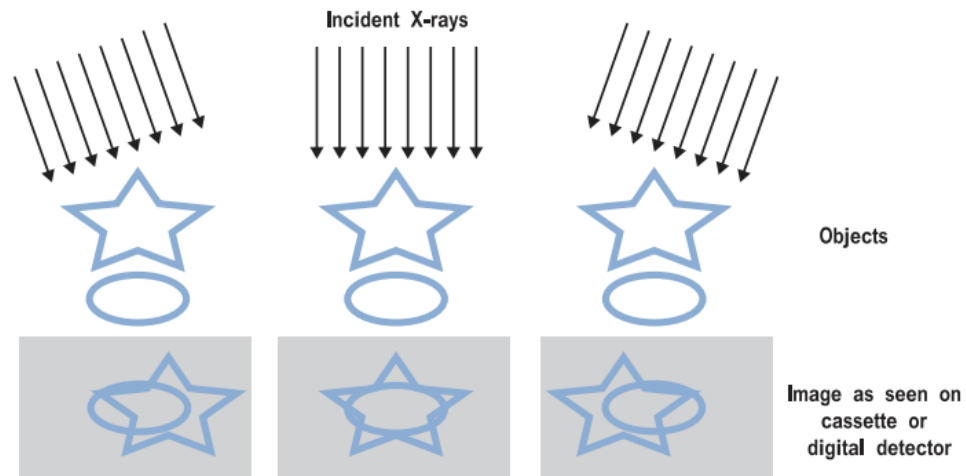


Figure 1.3: The images are obtained from different view separating structures at differing heights in tomosynthesis imaging [2].

When the system takes a conventional mammogram under the same compression, the tomosynthesis slices and the mammogram are simultaneously formed by completely making objects relevant in the two different image sets. Biopsy tissue sampling methods can easily be implemented in finding the right coordinates by using the tomosynthesis, because the location of an interested lesion in a slice obtained by using tomosynthesis completely finds its true 3D coordinate within the breast. If two calcifications are observable in the digital mammogram, the distance between the microcalcifications can be measured at the tomosynthesis slices. This 3D information is not available in normal mammography [2].

Breast CT and tomosynthesis are both designed to reduce the overlapping structures leading to fewer false positive findings. In breast CT, multiple 2-D projection images are acquired and then reconstructed to form true three-dimensional (3-D) images, which can be viewed in the transverse, sagittal, and coronal planes. In tomosynthesis, a limited angle scan is used to obtain 30–60 mammograms to reconstruct thick layer tomographic images in parallel to the detector. Tomosynthesis is more similar to digital mammography than breast CT. The similarity to mammographic images will likely lead to a shorter learning curve for interpreting tomosynthesis images when compared to cone-beam breast CT images. As tomosynthesis images are obtained with limited angular sampling, concerns have

been raised about the out-of-plane artifacts and the ability to visualize calcifications [72,73].

Gong et al. performed a computer simulation study with simulated lesions embedded into a 3-D breast model [74]. The authors evaluated lesion detection accuracy with digital mammography, tomosynthesis, and breast CT. The same total dose was used in the tomosynthesis and the breast CT simulations. A Receiver Operating Characteristic (ROC) study was performed with five physicist observers. The average area under the ROC curves was 0.76 for digital mammography, 0.93 for tomosynthesis, and 0.94 for breast CT. Both tomosynthesis and cone-beam breast CT provided statistically significant higher lesion detectability than digital mammography. The improved performance of breast CT and tomosynthesis compared to digital mammography may be based on the decreased image clutter, which resulted in improved tumor visibility. Lesion detectabilities for tomosynthesis and cone-beam CT were not statistically significantly different from each other. It should also be noted that in the study by Gong et al. breast compression was used in digital mammography and tomosynthesis but not generally in breast CT [74]. Without compression, higher kVp settings were needed, resulting in lower subjective breast tumor contrast [6].

1.6 Hypothesis

Detecting tumor is hard in breast tomography because of properties of breast tissues. A number of images are obtained at different views in tomosynthesis. The objects at different heights in the substances like breast tissues are projected differently in the different projections. Therefore, it is effective for screening lesion. Algebraic reconstruction techniques are generally used for reconstruction of the projections in tomosynthesis. The purpose of this work is to implement Algebraic reconstruction technique (ART) and Multiplicative Algebraic reconstruction technique (MART). In this study, two 3D phantom models were used. The original purpose of this thesis is to find an efficient algebraic reconstruction technique for out-of-focus slice blur problem in tomosynthesis imaging. Each implementation is inserted in Siddon's algorithm to take projections from using 3D phantoms and the coding is performed in C++.

2. METHODS

2.1 Siddon's Algorithm

In 1985, Siddon formulated a fast and accurate algorithm for 3D object to calculate the length while the ray goes from x-ray source through the image array. The principle is simple, but it requires high computation time. The computation time depends on the number of the planes of the 3D image array instead of the number of voxels of the 3D image [9].

The radiological path is represented as;

$$d = \sum_i \sum_j \sum_k l(i, j, k) p(i, j, k) \quad (2.1)$$

where $p(i, j, k)$ is the voxel density (attenuation coefficient) and the length parameter, $l(i, j, k)$, is the length of a line included by this voxel.

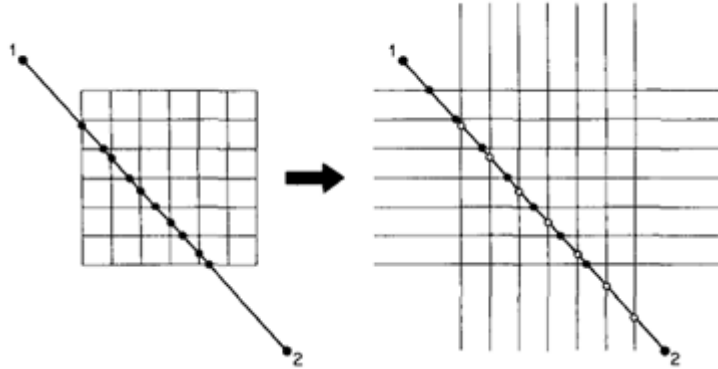


Figure 2.1: Geometric illustration of a ray on image grid [9].

Equation (2.1) is evaluated as an algorithm scaling with the number of terms according to the number of voxels in 3D space. Instead of considering them as independent elements, the voxels are assumed to be intersection volumes of equidistant parallel planes. The intersection points of the ray with the planes are calculated with the information of the intersection point of the ray with the first plane. Other intersection points of that ray with all the others are generated by

recursion. In Figure 2.1, the 2D version of the method is illustrated to understand simply. The pixels are considered as the intersection areas of equally spaced parallel planes in the figure.

Figure 2.1 shows that intersection points are the union of two sets. One of the sets includes the intersections of the ray with the horizontal lines (open circles) and the other with the vertical lines (closed circles). It is obvious that the intersections with the pixels are a subset of intersections with the lines. The subset provides to determine the radiological path.

In Siddon's algorithm, a ray from the start point located on (x_1, y_1, z_1) to the end point located on (x_2, y_2, z_2) is symbolized linearly by;

$$\begin{aligned} X(a) &= X_1 + \alpha(X_2 - X_1), \\ Y(a) &= Y_1 + \alpha(Y_2 - Y_1), \\ Z(a) &= Z_1 + \alpha(Z_2 - Z_1), \end{aligned} \quad (2.2)$$

where the parameter α is zero at start point and unity at end point. An α parameter in the range of $(\alpha_{\min}, \alpha_{\max})$ is used in evaluating each intersection. Even if start point or end point lie on outside of the image array, the first and last intersection points will take the parameters α_{\min} and α_{\max} respectively.

For a $(N_x - 1, N_y - 1, N_z - 1)$ voxels image array, the orthogonal sets of equidistant parallel planes are written as;

$$\begin{aligned} X_{plane}(i) &= X_{plane}(1) + (i - 1)d_x, & (i = 1, 2, \dots, N_x) \\ Y_{plane}(j) &= Y_{plane}(1) + (j - 1)d_y, & (j = 1, 2, \dots, N_y) \\ Z_{plane}(k) &= Z_{plane}(1) + (k - 1)d_z, & (k = 1, 2, \dots, N_z) \end{aligned} \quad (2.3)$$

where d_x , d_y and d_z are the distances between the planes. They are also the size of the voxel. The maximum and minimum values for the α parameter are evaluated with intersecting the ray with the sides of the image array. The parametric values of the sides are calculated from Equations (2.2) and (2.3) as follows;

If $(X_2 - X_1) \neq 0$,

$$\begin{aligned} \alpha_x(1) &= \lfloor X_{plane}(1) - X_1 \rfloor / (X_2 - X_1), \\ \alpha_x(N_x) &= \lceil X_{plane}(N_x) - X_1 \rceil / (X_2 - X_1), \end{aligned} \quad (2.4)$$

Equations for y and z directions are similar. Minimum and maximum values of α (α_{\min} , α_{\max}) depend on the location of the start and end point. The values are computed by merging the sets as in Equation (2.5),

$$\begin{aligned} a_{\min} &= \max\{0, \min[\alpha_x(N_x)], \min[\alpha_y(1), \alpha_y(N_y)], \min[\alpha_z(1), \alpha_z(N_z)]\} \\ a_{\max} &= \min\{1, \max[\alpha_x(N_x)], \max[\alpha_y(1), \alpha_y(N_y)], \max[\alpha_z(1), \alpha_z(N_z)]\} \end{aligned} \quad (2.5)$$

The ray does not intersect the image array if α_{\max} is less than or equal to α_{\min} . The range of indices (i_{\min}, i_{\max}), (j_{\min}, j_{\max}), and (k_{\min}, k_{\max}) intersected planes having parametric values in the range (α_{\min} , α_{\max}) are achieved as follows;

If $(X_2 - X_1) \geq 0$,

$$\begin{aligned} i_{\min} &= N_x - [X_{line}(N_x) - \alpha_{\min}(X_2 - X_1) - X_1] / d_x \\ i_{\max} &= 1 + [X_1 + \alpha_{\max}(X_2 - X_1) - X_{line}(1)] / d_x \end{aligned} \quad (2.6)$$

If $(X_2 - X_1) \leq 0$,

$$\begin{aligned} i_{\min} &= N_x - [X_{line}(N_x) - \alpha_{\max}(X_2 - X_1) - X_1] / d_x \\ i_{\max} &= 1 + [X_1 + \alpha_{\min}(X_2 - X_1) - X_{line}(1)] / d_x \end{aligned}$$

with similar equations hold for j_{\max} , j_{\min} , k_{\min} and k_{\max} .

The sets of parametric values represent the intersections of the ray with all the planes. The sets can be given including the indice data using the notation for $\{\alpha_x\}$ and with similar notations for $\{\alpha_y\}$, $\{\alpha_z\}$;

$$\begin{aligned} \{a_x\} &= \{a_x(i_{\min}), \dots, a_x(i_{\max})\}; & X_2 - X_1 > 0 \\ \{a_x\} &= \{a_x(i_{\max}), \dots, a_x(i_{\min})\}; & X_2 - X_1 < 0 \end{aligned} \quad (2.7)$$

where

$$\begin{aligned} a_x(i) &= [X_{line}(i) - X_1] / (X_2 - X_1) \\ &= a_x(i-1) + [d_x / (X_2 - X_1)] \end{aligned} \quad (2.8)$$

The definite intersection points are obtained by merging the sets $\{\alpha_x\}$, $\{\alpha_y\}$ and $\{\alpha_z\}$ into one set. The minimum and maximum values are also added to the merged set as the first and last elements respectively.

$$\begin{aligned} \{a_x\} &= \{a_{\min}, \text{merge}[\{\alpha_x\}, \{\alpha_y\} \text{ and } \{\alpha_z\}], \alpha_{\max}\}; \\ &= \{\alpha(0), \dots, \alpha(n)\} \end{aligned} \quad (2.9)$$

where index n is given as ;

$$n = (i_{\max} - i_{\min} + 1) + (j_{\max} - j_{\min} + 1) + (k_{\max} - k_{\min} + 1) \quad (2.10)$$

For two intersections m and $m-1$, the intersection length of the voxel is defined as;

$$l(m) = d_{12} [\alpha(m) - \alpha(m-1)], \quad (m = 1, \dots, n) \quad (2.11)$$

The mid point of the two adjacent intersections, m and $m-1$, is calculated the voxel indices $[i(m), j(m), k(m)]$ by the following equation;

$$\begin{aligned} i(m) &= 1 + \lfloor [X_1 + \alpha_{mid} (X_2 - X_1) - X_{plane}(1)] / d_x \rfloor \\ j(m) &= 1 + \lfloor [Y_1 + \alpha_{mid} (Y_2 - Y_1) - Y_{plane}(1)] / d_y \rfloor \\ k(m) &= 1 + \lfloor [Z_1 + \alpha_{mid} (Z_2 - Z_1) - Z_{plane}(1)] / d_z \rfloor \end{aligned} \quad (2.12)$$

where α_{mid} is given by

$$\alpha_{mid} = [\alpha(m) + \alpha(m-1)] / 2 \quad (2.13)$$

In Equation (2.1) the radiological path can be finally written as;

$$\begin{aligned} d &= \sum_{m=1}^n l(m) p[i(m), j(m), k(m)] \\ &= d_{12} \sum_{m=1}^n [\alpha(m) + \alpha(m-1)] p[i(m), j(m), k(m)] \end{aligned} \quad (2.14)$$

where $p(i, j, k)$ defines the voxel intensity. The main advantage of this algorithm is its computation time that is scaled with the number of the planes (N) instead of the number of voxels (N^3) [9].

2.2 Algebraic Reconstruction Technique

The Algebraic Reconstruction Technique (ART) is an iterative image reconstruction with a long history and rich literature. Firstly, Kaczmarz designed it in 1937 [17]. It was independently used by Gordon et al. in image reconstruction [18]. ART is a row-action reconstruction algorithm that uses a

set of projections to reconstruct the desired object [19-21]. The technique is accepted as an alternative solution to the limited angle reconstruction problem. It works readily for asymmetric objects and produces the detail of such objects with limited views. The term ray-sum can be used instead of the line integral in transform-based methods. The ray-sum, p_i , measured with the i th ray, is expressed as;

$$\sum_{k=1}^N w_{ik} \cdot f_k = p_i \quad \begin{array}{l} (i = 1, 2, \dots, M) \\ (k = 1, 2, \dots, N) \end{array} \quad (2.15)$$

where w_{ik} is the weighting parameter which stands for the influence of k th cell on the i th ray line integral, f_k is the constant intensity value of the k th cell and M is the total number of rays.

Finding the solution via subsequent projections is known as the method. A linear imaging problem such as tomography can be shown as below,

$$Y = AX, \quad (2.16)$$

where Y represents observations, A represents an $M \times N$ system matrix and X shows the unknowns. ART method works with updating in each iteration. An initial guess is necessary for the implementation of the technique. $\vec{f}^{(0)}$ is projected on the first plane in Equation (2.15) giving $\vec{f}^{(1)}$. Then $\vec{f}^{(1)}$ is projected on the second plane giving $\vec{f}^{(2)}$, and so on. This procedure can be formulated as projection of $\vec{f}^{(i-1)}$ on i th plane yields $\vec{f}^{(i)}$;

$$f_j^{(i)} = f_j^{(i-1)} + \frac{p_i - \sum_{k=1}^N f_k^{(i-1)} \cdot w_{ik}}{\sum_{k=1}^N w_{ik}^2} w_{ij} \quad \begin{array}{l} (i = 1, 2, \dots, M) \\ (j = 1, 2, \dots, N) \end{array} \quad (2.17)$$

Equation (2.17) states that the previous intensity values of the estimated image, $\vec{f}_j^{(i-1)}$ are updated by adding an error parameter $\Delta f_j^{(i)}$. The parameter is obtained by calculating the difference between measured ray-sum, p_i , and the computed ray-sum, $\sum_{k=1}^N f_k^{(i-1)} \cdot w_{ik}$, normalizing the difference by $\sum_{k=1}^N w_{ik}^2$. Update process is repeated until all the projections and iterations are done [7, 8].

2.3 Multiplicative Algebraic Reconstruction Technique

MART (multiplicative algebraic reconstruction technique) is a nonlinear iterative algorithm for CT image reconstruction [75]. It has two features: the first one is relative to the solution of underdetermined set of linear CT equations causing entropy [76-78], and the second one is about the limitation of the reconstruction to the convex hull of the object [10,79-81]. In the MART, a multiplicative correction is required for the voxel intensity in each iteration k , based on the ratio of the recorded p_i to the projected $\sum_j w_{ij} f_j^k$ pixel intensity, expressed as

$$f_j^{(i)} = f_j^{(i-1)} \left(\frac{p_i}{\sum_i w_{ij} f_j^{(i-1)}} \right)^{\mu w_{ij}} \quad \begin{array}{l} (i = 1, 2, \dots, M) \\ (j = 1, 2, \dots, N) \end{array} \quad (2.18)$$

where i is the iteration number and μ is a relaxation parameter typically chosen between 0 and 2 [75] and for the stability, less than one is preferred [82]. In addition, μw_{ij} is represented as power (p) in this study.

Until the iteration is completed, the intensity of each voxel is corrected. By means of this method, the entropy solution-focused information is converged [12]. While the MART is considered appropriate for the first estimations, as Elsinga et al. [13] demonstrate, this algorithm have the precedence over that of additive algebraic reconstruction technique (ART) [11].

The algorithm provides solution for the problem of tomographic reconstruction of high-contrast objects on a dark background, such as the diffraction-limited particle images. When compared to the other algebraic reconstruction techniques, the MART suggests the most useful solutions in the reconstruction of sparse distributions involving high spatial frequencies such as those of the diffraction-limited particle images Elsinga et al. introduces the main factors effecting the accuracy of the reconstruction process; the first is the number of viewing cameras, and the second is the image source density [13]. The other elements effecting the accuracy of reconstruction are the viewing angle, the width and intensity distribution of the illuminated domain and the amount of background and spurious light [15].

Although the performance of MART algorithm in the reconstruction quality in fewer iterations is better than the other algebraic reconstruction techniques, the long reconstruction times and large computer memory allocations must be taken into consideration [11,16].

3. RESULTS

In this thesis 3D image reconstruction with a ray-tracing algorithm which is Siddon's method, evaluating the radiological path of a ray through a 3D object, is studied in algebraic reconstruction techniques. The projection images are obtained from different angles [9] and reconstructed by using algebraic reconstruction technique (ART) and multiplicative algebraic reconstruction technique (MART).

A 3-D phantom that is Shepp–Logan phantom was selected to test the performance of the reconstruction algorithms of tomosynthesis imaging system. The Shepp–Logan phantom is a standard test image created by Larry Shepp and Benjamin F. Logan and serves as the model of a human head in the development and testing of image reconstruction algorithms. Phantom data sets consist of two ellipsoids with a low attenuation coefficient ($\mu=1,73472\times 10^{-12}$) at the lower part of the phantom. Forward projection is done between -25 and +25 degrees with 11 exposures that happen in each 5 degrees. The projection files were created by forward projecting, which are used as generated projection images to do the reconstruction using ART and MART. Equation (3.1) is used to rotate x-ray source and detector coordinates.

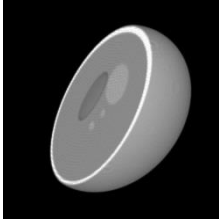
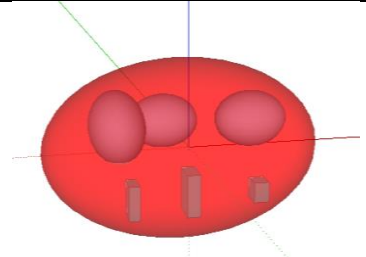
$$R_y(\theta) = \begin{bmatrix} \cos \theta & 0 & \sin \theta \\ 0 & 1 & 0 \\ -\sin \theta & 0 & \cos \theta \end{bmatrix} \quad \theta = [0, \pi] \quad (3.1)$$

where θ is the given rotation angle. The time needed to perform a simulation study depends on the complexity of the chosen sets of source, detector and objects. The average time ranges in turn are as followed: 36ms for completing one projection , 5.587 s for displaying 11 projection images, 479ms for reconstruction of the tomosynthesis system.

Another 3-D phantom was designed more complex than the other to test the performance of the reconstruction algorithms. Phantom data sets consist of three objects which are rectangular prism with low attenuation coefficient at the lower part of the phantom and three ellipsoid in the upper part of the phantom with high attenuation coefficient. Attenuation coefficients are scaled between 0 and 15. It must

be taken into account that the small object is obscured with the larger object in the phantom. Forward projection is done between -25 and +25 degrees with 11 exposures that happen in each 5 degrees. Parameters of phantoms are shown in Table 3.1 below.

Table 3.1: Phantoms parameters.

Parameter Name	Value	
	PHANTOM I	PHANTOM II
Number of layers (z-axis)	51	16
Dimensions on x-y axis	64×64	128×128
Dimensions of detector	160×160	160×160
Coordinates of detector	(0,0,-100)	(0,0,-100)
Coordinates of x-ray source	(0,0,200)	(0,0,200)
Objects in phantoms	2 Ellipsoids	3 Rectangular Prisms and 3 Ellipsoids
Figure of Phantom		

Firstly, different exponents $\mu = \{0.5, 1\}$ are assumed as the μ of MART, called as method I. Secondly, the other method called method II is defined by multiplied by maximum of all w_{ik} and w_{jk} . Parameters of MART are shown in Table 3.2 below.

Table 3.2: MART parameters.

Method No	Power (p)
Method I	$\{0.5 * w_{ik}, 1 * w_{jk}\}$
Method II	$1/\max \{ w_{ik} \mid i=1, \dots, I, j=1, \dots, J \}$

The images of LOI of phantom I and phantom II are shown in Figure 3.1 and Figure 3.2, respectively to compare each image obtained by implementing the reconstruction algorithms.

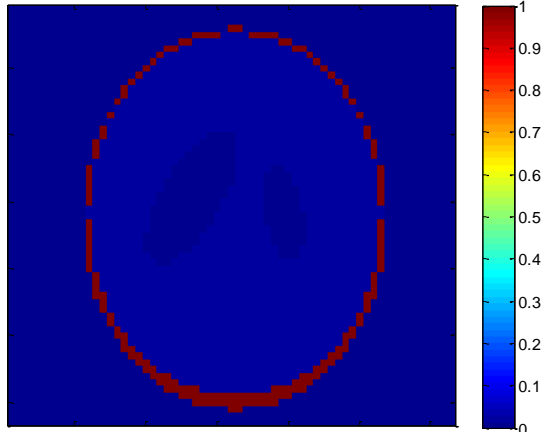


Figure 3.1: LOI image of phantom I.

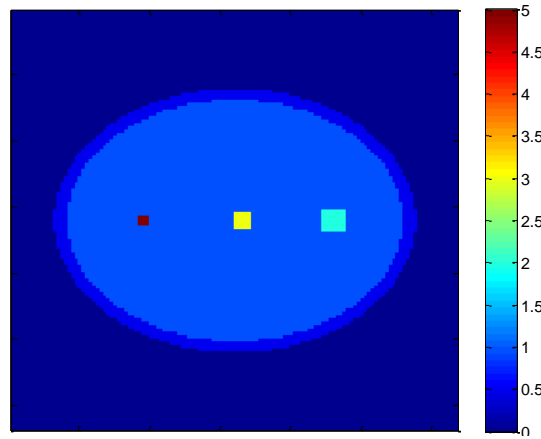


Figure 3.2: LOI image of phantom II.

Root mean square error (RMSE), Contrast to Noise Ratio (CNR) and Mean Structural SIMilarity (MSSIM) are calculated as in Equation (3.2), (3.3) and (3.6) and are used to compare each reconstructed image.

$$RMSE = \sqrt{\frac{1}{N} \sum_{i=1}^N (\hat{\mu}_i - \mu_i)^2} \quad (3.2)$$

where μ and $\hat{\mu}$ are original and estimated coefficient of attenuation for voxels, respectively and N is number of pixel.

$$CNR = \frac{\frac{1}{N} \sum_{i=1}^N \hat{\mu}_i - \frac{1}{N} \sum_{i=1}^N \bar{\mu}_i}{\sigma(\bar{\mu}_i - \mu_i)} \quad (3.3)$$

where μ , $\bar{\mu}$, and $\hat{\mu}$ are background of original, background of estimated, and estimated coefficient of attenuation for voxels, respectively and N is number of pixel.

The root mean square error (RMSE) is generally used for measuring the image quality. It has a common usage because of being simple for calculating clear physical meaning. However, RMSE is not an appropriate metric to exhibit the visual quality of the images [22-24]. Human visual system characteristics are used by several quality assessment methods. SSIM is one of the well-known measurement methods of them. It compares local patterns of pixel values of images which are normalized for amount of contrast and luminance [25].

The SSIM index is shown as:

$$SSIM(x, y) = \frac{(2\mu_x\mu_y + C_1)(\sigma_{xy} + C_2)}{(\mu_x^2 + \mu_y^2 + C_1)(\sigma_x^2 + \sigma_y^2 + C_2)} \quad (3.4)$$

where μ_x and μ_y refer to mean of the intensities of signals x and y, respectively and σ_x and σ_y are the standard deviation of them. C_1 and C_2 are given below,

$$C_i = (K_i L)^2, \quad (i = 1, 2) \quad (3.5)$$

where L is the dynamic range of the pixel values and $K_1 \ll 1$ and $K_2 \ll 1$ are small constants.

A single quality measurement of the whole image is practically necessary. The mean SSIM (MSSIM) index is used for evaluating the image quality

$$MSSIM(X, Y) = \frac{1}{M} \sum_{i=1}^M SSIM(x_i + y_i) \quad (3.6)$$

where X and Y relate to original and reconstructed image, respectively; x_i and y_i are the image values at the ith pixel and M is the number of pixels in the image.

3.1 Results of Phantom I

The study was implemented by performing projections and reconstruction tasks to exhibit reconstructed layer of interest. The reconstructed images of 29th layer of the phantom are obtained using ART and MART with different power values. The difference among the results in Figure 3.3 is not clear. For comparison of the images, RMSE and MSSIM values are calculated. CNR value is not evaluated because of the complexity of Phantom I.

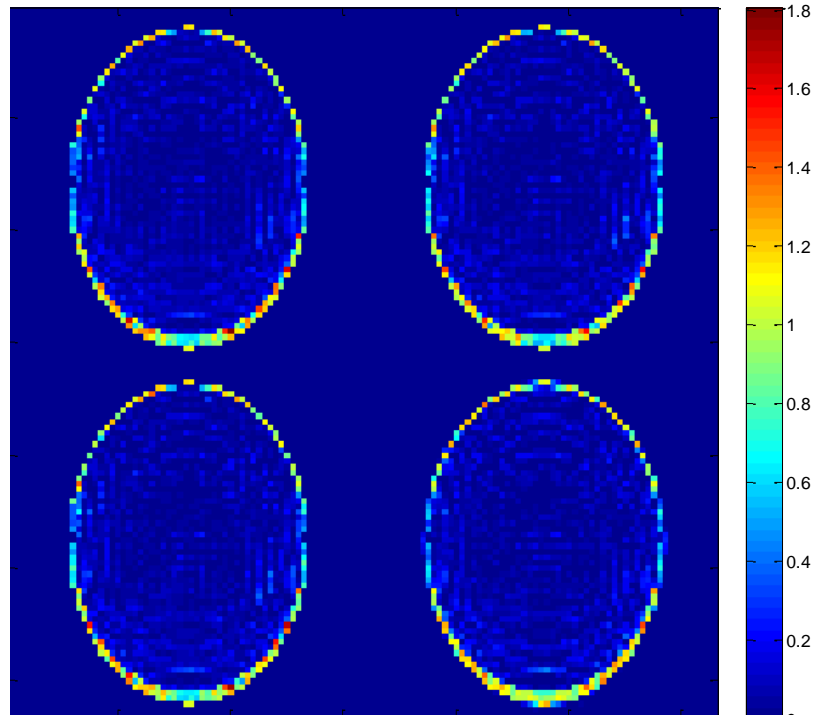


Figure 3.3: Images of the LOI (29th layer of the phantom) upper row from left to right shows the reconstructed LOI image using MART ($p= 0.5$, method I), using MART ($p= 1$, method I), and bottom row from left to right shows using MART (method II), using ART.

Figure 3.4 shows the comparison of the root mean square error (RMSE) values in MART with the different parameters and ART after 15 iterations. RMSE value decreases while the iteration number increases. Although ART has less RMSE value than the others in the beginning of iterations, MART method I ($p=1$) and method II have the minimum RMSE value after 15 iterations.

As shown in Figure 3.5, increasing the number of iterations leads to the increase in the MSSIM value. During the period MSSIM, the value of ART is almost steady and high value. MSSIM values of MART with different parameters rapidly increase in the beginning of the iterations. After 5 iterations, MSSIM value has slight increase. Especially, MSSIM values of MART method I ($p=1$) and MART method II reached the value obtained by using ART. In addition, as shown in Figure 3.4 and Figure 3.5, MART method I ($p=1$) and MART method II are almost identical.

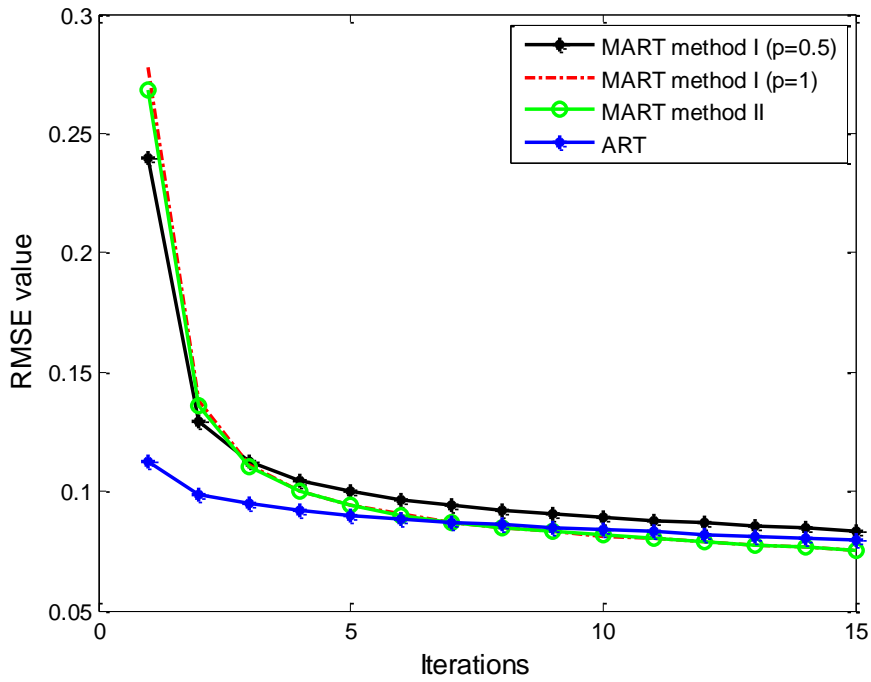


Figure 3.4: RMSE value comparison of MART ($p=0.5$, method I), ($p=1$, method I), (method II), and ART for phantom I.

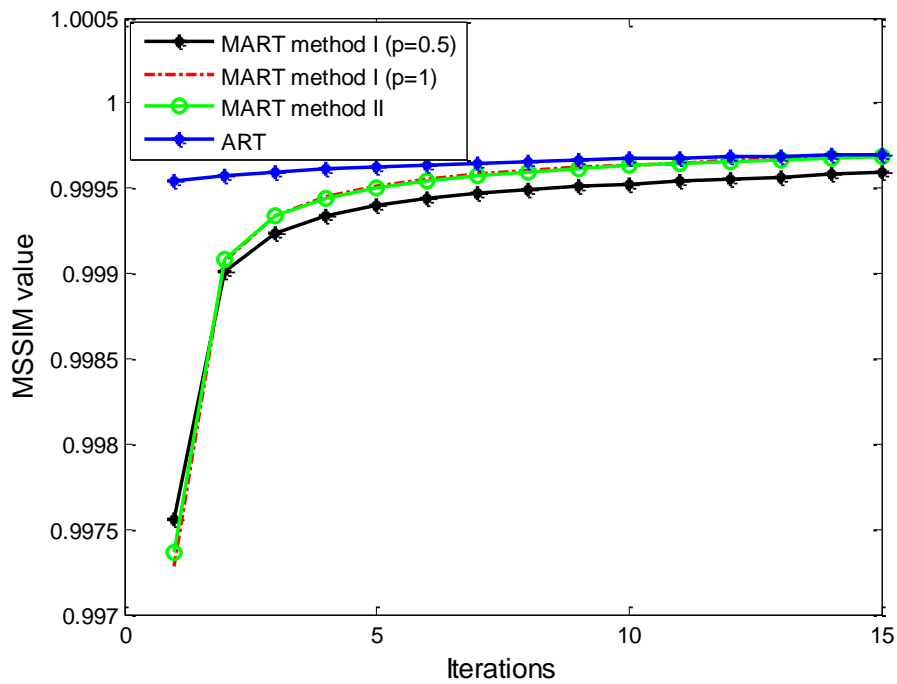


Figure 3.5: MSSIM value comparison of MART ($p=0.5$, method I), ($p=1$, method I), (method II), and ART for phantom I.

3.2 Results of Phantom II

ART and MART with two methods are implemented in Phantom II. It is done between -25 and +25 degrees with 11 exposures that happen in each 5 degrees. Reconstructed images of 11th layer of the phantom are obtained using ART and MART with different power values. As shown Figure 3.6, image reconstructed by using ART is more similar to original than the others.

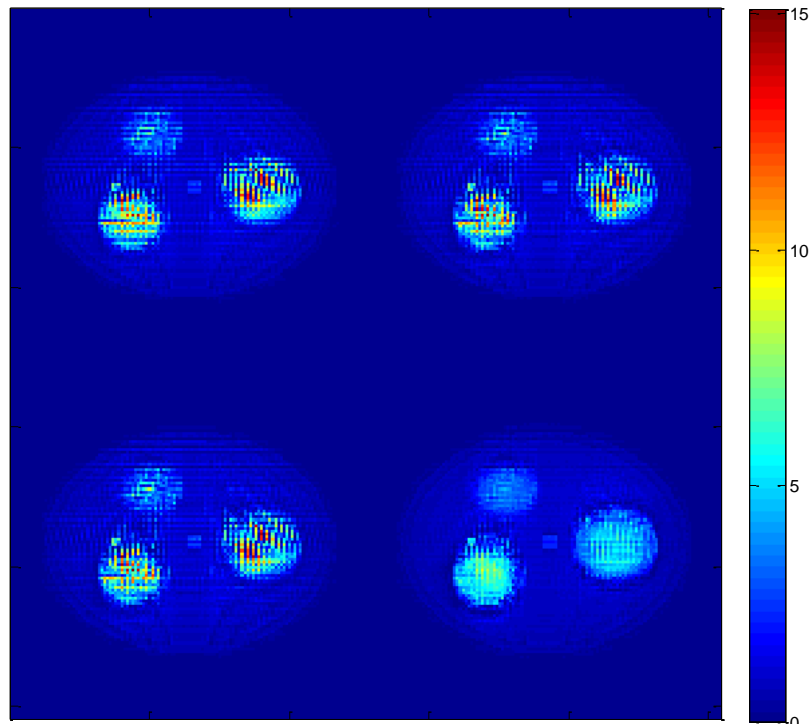


Figure 3.6: Images of the LOI (11th layer of the phantom) upper row from left to right shows the reconstructed LOI image using MART ($p= 0.5$, method I), using MART ($p= 1$, method I), and bottom row from left to right shows using MART (method II), using ART.

Figure 3.7 shows the comparison of the root mean square error (RMSE) values in MART with the different parameters and ART after 15 iterations for phantom II. RMSE value decreases while the iteration number increases. ART has the minimum RMSE value in all iterations. RMSE values obtained from MART method I ($p=1$) and method II exceed that of MART method I ($p=0.5$) for the first iteration, but since then there has been steady decline in RMSE value from MART method I ($p=1$) and method II.

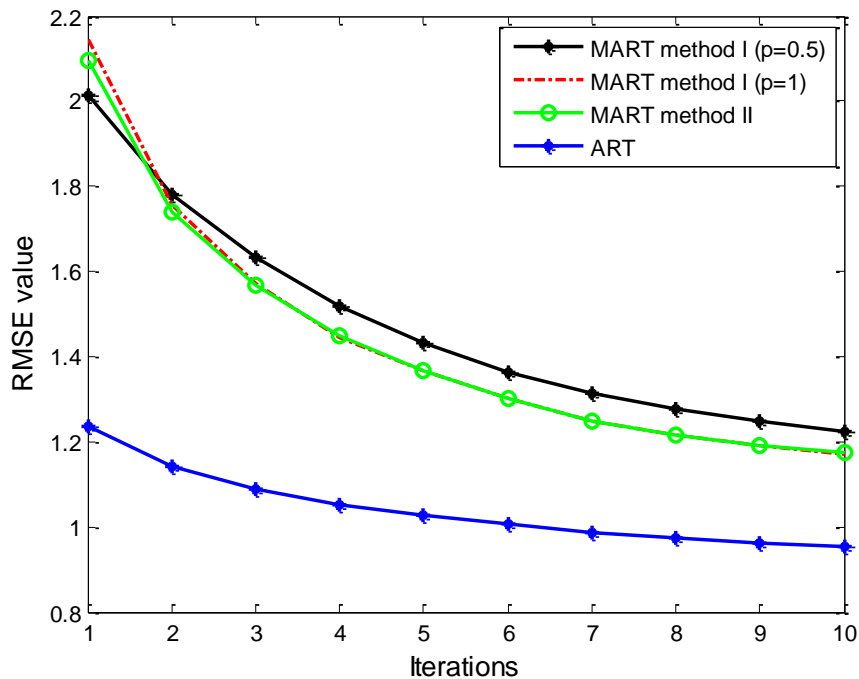


Figure 3.7: RMSE value comparison of MART ($p=0.5$,method I), ($p=1$,method I), (method II), and ART for phantom II.

In Figure 3.8 there has been a gradual increase in CNR value of MART ($p=0.5$,method I) during the period. In 8th iteration, CNR values of MART method I ($p=1$) and method II exceed that of ART. After that, there has been a steady increase in CNR values of MART method I ($p=1$) and method II, which seems to continue.

MSSIM value of ART has the highest value over the period as shown Figure 3.9. MSSIM values obtained from MART method I ($p=1$) and method II exceed that of MART method I ($p=0.5$) for the first iteration. Therefore, there has been gradual increase in MSSIM value from MART method I ($p=1$) and method II.

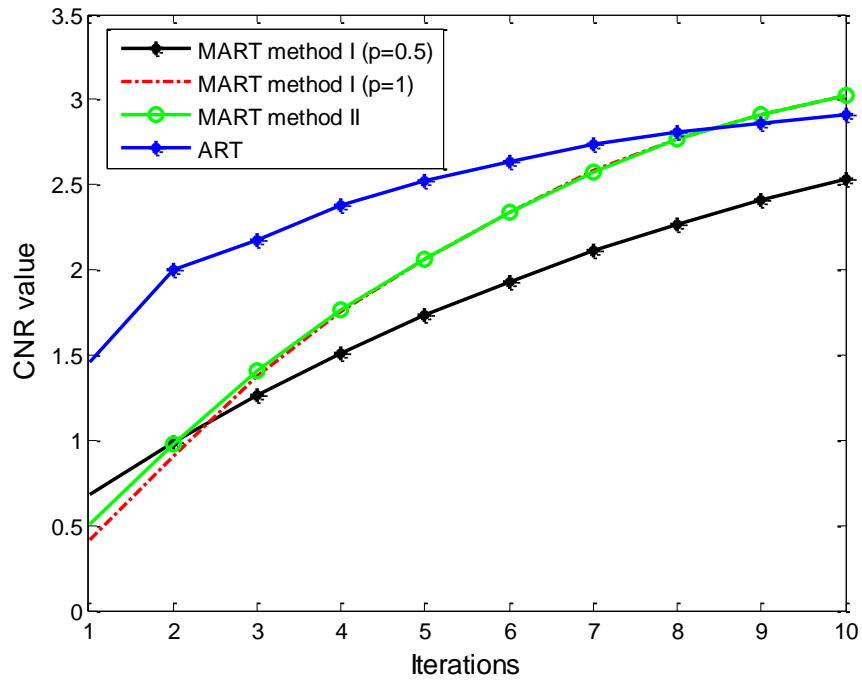


Figure 3.8: CNR value comparison of MART ($p=0.5$,method I), ($p=1$,method I), (method II), and ART for phantom II.

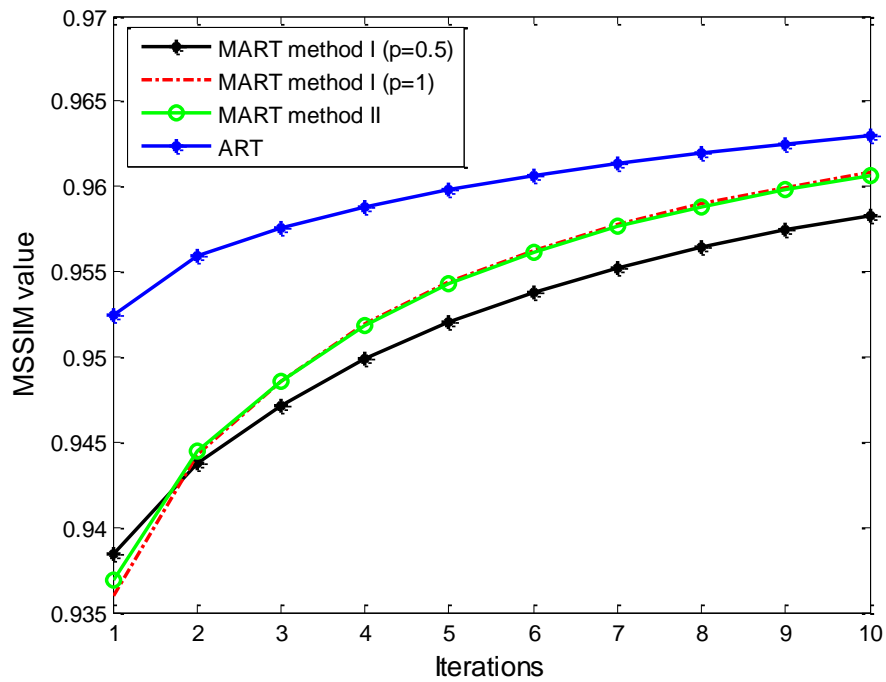


Figure 3.9: MSSIM value comparison of MART ($p=0.5$,method I), ($p=1$,method I), (method II), and ART for phantom II.

3. DISCUSSION

Obtained projection images by using Siddon algorithm were reconstructed into 3D phantom by using ART and MART with different exponents. In the results of Phantom I, MART gives better result compared to RMSE value, but ART has better result than MART algorithm for MSSIM value. Atkinson and Soria (2007) supposed that the MART method I ($p=1$) and method II algorithms have better reconstruction quality in fewer iterations when the algorithms were compared with ART. It is really true that MART quickly converges almost the same result of ART. Although it is thought that MART requires long times for reconstruction and large memory allocations on computer, computation times of both algorithms are almost identical, approximately 13 minutes. In addition, for phantom II ART has better RMSE and MSSIM values than MART with different power parameters. On the other hand, CNR values of the MART method I ($p=1$) and method II are better than that of ART for Phantom II. The difference between the results of both phantoms may be explained by using different μ in equation of MART, but it is difficult to decide optimum power parameter for any phantom.

Applying different exponents in MART affected the reconstructed images. MART method I ($p=1$) and method II have better result than the other MART method. The power parameter can be optimized for any tomosynthesis system. For a better result, the number of iterations can be increased in the implementation of algorithms. Also, ART and MART are applied two different designed phantoms. The algorithms can be applied on more different phantoms to investigate their behaviours. Phantoms were designed with respect to be considered as breast tissues. Moreover, real breast phantoms should be used for showing the applicability of algorithms in real.

4. CONCLUSION

Breast cancer is the most common cancer type among female diseases all over the world. Early diagnosis and treatment is especially important in reducing the death rate since the causes of breast cancer are unknown. Tomosynthesis, which is a method of 3D imaging, can reduce the tissue overlap effect. Advantages of the digital tomosynthesis device includes the possibility of reduced breast compression, improved diagnostic and screening accuracy, 3D lesion localization, and the contrast enhanced 3D imaging. Also, the coordinates of suspicious tissues are found because the location of a lesion in a tomosynthesis slice completely finds its true 3D coordinate within the breast. In this study, Siddon algorithm is used for the projection of designed 3D phantoms such as breast. Obtained from the projections of phantoms are reconstructed into ART and MART with different power parameters. The out of focus blur in the reconstructed image using ART and MART was reduced for limited scan angle tomosynthesis. RMSE, CNR and MSSIM values were used to decide which method is the best. MART gives better result according to RMSE value for phantom I. On the other hand, ART has better RMSE and MSSIM values than that of MART with the best parameters for phantom II. In addition, computation times of both algorithms are almost identical.

REFERENCES

- [1] **American Cancer Society.** (2012). Breast Cancer Facts & Figure.
- [2] **Andrew P. Smith , Patricia A. Hall, Donna M. Marcello.** (2006). Emerging Technologies in Breast Cancer Detection, Hologic.
- [3] **Cheng H. D., Cai X., Chen X.** (2003). Computer-aided detection and classification of micro-calcifications in mammograms: a survey. *Pattern Recognition*, 36(12):2967 – 2991.
- [4] **Cheng H. D., Shi X. J., and Min R.** (2006). Approaches for automated detection and classification of masses in mammograms. *Pattern Recognition*,39(4):646 –668.
- [5] **Wushuai J., Xueyan S. and Shuqian L.** (2012). Computer-aided diagnosis of breast microcalcifications based on dual-tree complex wavelet transform. *BioMedical Engineering OnLine* 2012, 11:96
- [6] **William R. Hendee, Series Editor.** (2013). *Physics of Mammographic Imaging*, pp. 3-9.
- [7] **Wang B., Kenneth B., and Denny Lee.** (2004). Algebraic Tomosynthesis Reconstruction. *Medical Imaging*, pp. 711-717.
- [8] **Kak A. C. and Slaney M.** (1988). *Principles of Computerized Tomographic Imaging*. IEEE Press.
- [9] **Siddon R. L.** (1985). Fast calculation of the exact radiological path for three dimensional CT array. *Medical Physics*, Mar/Apr, pp. 252-255.
- [10] **Cristian Badea and Richard Gordon.** (2004). Experiments with the nonlinear and chaotic behaviour of the multiplicative algebraic reconstruction technique (MART) algorithm for computed tomography. *Physics in medicine and biology*, vol. 49.
- [11] **Atkinson C. H. and Soria.** (2007). Algebraic Reconstruction Techniques for Tomographic Particle Image Velocimetry. 16th Australasian Fluid Mechanics Conference Crown Plaza, Gold Coast.
- [12] **Lent, A.** (1976). Maximum entropy and the multiplicative art. in *Proc. Conf. Image Analysis and Evaluation*, SPSE, Toronto.
- [13] **Elsinga, G. E., Scarano, F., Wieneke, B. and van Oud-heusden, B. W.** (2006). Tomographic particle image velocimetry, *Experiments in Fluids*, 41, 933–947.
- [14] **Stefano Discetti and Tommaso Astarita.** (2011). A fast multi-resolution approach to tomographic PIV. Springer-Verlag.

- [15] **Scarano F. and Poelma C.** (2009). Three-dimensional vorticity of cylinder wakes. Springer.
- [16] **Buchmann N. A., Atkinson C., Jeremy M. C., and Soria J.** (2011). Tomographic particle image velocimetry investigation of the flow in a modeled human carotid artery bifurcation. Springer.
- [17] **S. Kaczmarz.** (1937). Angenäherteauflösung von systemenlinearergleichungen. Bulletin de l'Académie Polonaise des Sciences etLettres, A35, 355–357.
- [18] **Herman G. T.** (1980). Image reconstruction from projections: the fundamentals of computerized tomography. Academic Press, New York, NY, USA.
- [19] **Censor Y. and Zenios S. A.** (1997). Parallel optimization: theory, algorithms, and Applications. Oxford University Press, New York, NY, USA.
- [20] **Nikazad T.** (2008). Algebraic reconstruction methods. Linköping Studies in Science and Technology. Dissertations. Thesis No. 1186.
- [21] **Raparia D., Alessi J., and Kponou A.** (1997). The algebraic reconstruction technique (Art). AGS Department, Brookhaven National Lab, Upton, NY 11973, USA.
- [22] **Girod B.** (1993). What's wrong with mean-squared error. Digital Images and Human Vision. A. B. Watson, Ed. Cambridge, MA: MIT Press, pp. 207–220.
- [23] **Teo P. C. and Heeger D. J.** (1994). Perceptual image distortion. Proc. SPIE, vol. 2179, pp. 127–141.
- [24] **Eskicioglu A. M. and Fisher P. S.** (1995). Image quality measures and their Performance. IEEE Trans. Commun., vol. 43, pp. 2959–2965, Dec.
- [25] **Wang Z., Bovik A. C., Sheikh H. R., and Simoncell E. P.** (2004). Image Quality Assessment: From Error Visibility to Structural Similarity. IEEE Trans. on Image Processing, Vol. 13, No. 4.
- [26] **Pisano D. J., David G. Barnes, Brad K. Gibson, Lister Staveley-Smith, Ken C. Freeman, and Virginia A. Kilborn.** (2004). Where are the high-velocity clouds in local group analogs. The Astrophysical Journal Letters, Vol. 610, Num. 1, ApJ, 610, L17
- [27] **Haus A. G, Doi K., Metz C. E., and Bernstein J.** (1997). Image quality in mammography. Radiology 125:77-85.
- [28] **Gisvold J. J., Karsell P. R., and Reese E. C.** (1977). Clinical evaluation of computerized tomographic mammography. Mayo Clin Proc. 52(3): 181–185
- [29] **Gisvold J. J., Reese D. F., and Karsell P. R.** (1979). Computed tomographic mammography (CTM). AJR Am J Roentgenol 133(6):1143–1149.
- [30] **Chang C. H. et al.** (1977). Computed tomography of the breast. A preliminary report. Radiology 124(3): 827–829.
- [31] **Chang C. H. et al.** (1978). Computed tomographic evaluation of the breast. AJR Am J Roentgenol 131(3): 459–464.

- [32] **Chang C. H. et al.** (1980). Computed tomography in detection and diagnosis of breast cancer. *Cancer* 46(4 Suppl): 939–946.
- [33] **Chang C. H. et al.** (1982). Computed tomographic mammography using a conventional body scanner. *AJR Am J Roentgenol* 138(3): 553–558.
- [34] **Muller J. W., van Waes P. F., and Koehler P. R.** (1983). Computed tomography of breast lesions: comparison with x-ray mammography. *J Comput Assist Tomogr* 7(4):650–654.
- [35] **Boone J. M. et al.** (2001). Dedicated breast CT: Radiation dose and image quality evaluation. *Radiology* 221(3): 657–667.
- [36] **O’Connell A. et al.** (2010). Cone-beam CT for breast imaging: Radiation dose, breast coverage, and image quality. *Amer J Roentgenol* 195(2): 496–509.
- [37] **Lindfors K. K. et al.** (2008). Dedicated breast CT: Initial clinical experience. *Radiology* 246(3): 725–733.
- [38] **Ning R. et al.** (2007). A novel cone beam breast CT scanner: System evaluation. In *Medical Imaging 2007: Physics of Medical Imaging*. Pts 1–3.
- [39] **Boone J. M., Kwan A. L. C., Yang K., Burkett G. W., Lindfors K. K., and Nelson T. R.** (2006). Computed tomography for imaging the breast. *Journal of Mammary Gland Biology and Neoplasia* 11:103–111.
- [40] **Chen B. and Ning R.** (2002). Cone-beam volume CT breast imaging: feasibility study. *Med Phys* 29(5): 755–770.
- [41] **Dobbins J. T. and Godfrey D. J.** (2003). Digital x-ray tomosynthesis: current state of the art and clinical potential. *Phys Med Biol* 48: R65–R106.
- [42] **Radon J.** (1917). Über die bestimmung von funktionen durch ihrd intergralwerte l ängs gewisser mannigfaltigkeiten. *Ber Verch Saechs Akad Wiss Leipzig Math Phys Kl* 69: 262–267.
- [43] **Ziedses des Plantes B. G.** (1932). Eine neue methode zur differenzierung in der roentgenographie (planigraphie). *Acta Radiol* 13: 182–192.
- [44] **Chen X., Xie H., Erkamp R., Kim K., Jia C., Rubin J. M., and O’Donnell M.** (2005). 3-D correlation-based speckle tracking. *Ultrason Imag* 27: 21–36.
- [45] **Mertelemeier T., Orman J., Haerer W., and Dudam M. K.** (2006). Optimizing filtered backprojection reconstruction for a breast tomosynthesis prototype device. *Proc SPIE* 6142: 131–142.
- [46] **Rakowski J. T. and Dennis M. J.** (2006). A comparison of reconstruction algorithms for C-arm mammography tomosynthesis. *Med Phys* 33(8): 3018–3032.
- [47] **Chen Y., Lo J. Y., Baker J. A., and Dobbins J. T. III.** (2006). Gaussian frequency blending algorithm with matrix inversion tomosynthesis (MITS) and filtered back projection (FBP) for better digital breast tomosynthesis reconstruction. *Proc SPIE* 6142:122–130.

- [48] **Godfrey D. J., McAdams H. P., and Dobbins J. T. III.** (2006). Optimization of the matrix inversion tomosynthesis (MITS) impulse response and modulation transfer function characteristics for chest imaging. *Med Phys* 33(3): 655–667.
- [49] **Zhang Y., Chan H., Sahiner B., Wei J., Goodsitt M. M., Hadjiiski L. M., Ge J., and Zhou C.** (2006). A comparative study of limited-angle cone-beam reconstruction methods for breast tomosynthesis. *Med Phys* 33(10): 3781–3795.
- [50] **Duryea J., Dobbins J. T. III and Lynch J. A.** (2003). Digital tomosynthesis of hand joints for arthritis assessment. *Med Phys* 30: 325–333.
- [51] **Godfrey D. J., Rader A., and Dobbins J. T. III.** (2003). Practical strategies for the clinical implementation of matrix inversion tomosynthesis. *Proc SPIE* 5030: 379–390.
- [52] **Godfrey D. J. and Dobbins J. T. III.** (2002). Optimization of matrix inversion tomosynthesis via impulse response simulations. In *RSNA 88th Scientific Assembly*.
- [53] **Badea C., Kolitsi Z., and Pallikarakis N.** (2001). A 3D imaging system for dental imaging based on digital tomosynthesis and cone beam CT. *Proc Int Feder Med Biol Eng* 2: 739–741.
- [54] **Godfrey D. J., Warp R. L., and Dobbins J. T. III.** (2001). Optimization of matrix inverse tomosynthesis. *Proc SPIE* 4320: 696–704.
- [55] **Warp R. J., Godfrey E. J., and Dobbins J. T. III.** (2000). Applications of matrix inverse tomosynthesis. *Proc SPIE* 3977: 376–383.
- [56] **Suryanarnyannan S., Karellas A., Vedantham S., Glick S. J., Orsi C. J., and Webber R. L.** (1999). Comparison of contrast-detail characteristics of tomosynthetic reconstruction techniques for digital mammography. *Radiology* 213: 368–369.
- [57] **Sone S., Kasuga T., Sakai F., Kawai T., Oguchi K., Hirano H., Li F., Kubo K., Honda T., Haniunda M., Takemura K., and Hosoba M.** (1995). Image processing in the digital tomosynthesis for pulmonary imaging. *Eur Radiol* 5: 96–101.
- [58] **Dobbins J. T. III.** (1990). Matrix inversion tomosynthesis improvements in longitudinal x-ray slice imaging. U.S. Patent #4,903,204. Assignee: Duke University.
- [59] **Sklebitz H. and Haendle J.** (1983). Tomoscopy: Dynamic layer imaging without mechanical movements. *AJR* 140: 1247–1252.
- [60] **Maidment A. D., Ullberg C., Lindman K., Adelöw L., Egerström J., Eklund M., Francke T., Jordung U., Kristoffersson T., Lindqvist L., Marchal D., Olla H., Penton E., Rantanen J., Solokov S., Weber N., and Westerberg H.** (2006). Evaluation of a photon-counting breast tomosynthesis imaging system. *Proc SPIE* 6142: 89–99.

- [61] **Niklason L. T., Christian B. T., Niklason L. E., Kopans D. B., Castleberry D. E., Opsahl-Ong B. H., Landberg C. E., Slanetz P. J., Giardino A. A., Moore R., Albagli D., DeJule M. C., Fitzgerald P. F., Fobare D. F., Giambattista B. W., Kwasnick R. F., Liu J., Lubowski S. J., Possin G. E., Richotte J. F., Wei C. Y., and Wirth R. F.** (1997). Digital tomosynthesis in breast imaging. *Radiology* 205: 399–406.
- [62] **Wu T., Moore R. H., Rafferty E. A., and Kopans D. B.** (2004). A comparison of reconstruction algorithms for breast tomosynthesis. *Med Phys* 9: 2636–2647.
- [63] **Chen Y., Lo J. Y., and Dobbins J. T. III.** (2004). Matrix inversion tomosynthesis (MITS) of the Breast: Preliminary Results. In *RSNA 90th Scientific Assembly*.
- [64] **Chen Y., Lo J. Y., and Dobbins J. T. III.** (2005). Impulse response analysis for several digital tomosynthesis mammography reconstruction algorithms. *Proc SPIE* 5745: 541–549.
- [65] **Wu T., Moore R. H., Rafferty E. A., and Kopans D. B.** (2004). A comparison of reconstruction algorithms for breast tomosynthesis. *Med Phys* 9: 2636–2647.8
- [66] **Stevens G. M., Fahrig R., and Pelc N. J.** (2001). Filtered backprojection for modifying the impulse response of circular tomosynthesis. *Med Phys* 28: 372–380.
- [67] **Lauritsch G and Haerer W.** (1998). A theoretical framework for filtered back-projection in tomosynthesis. *Proc SPIE* 3338: 1127–1137.
- [68] **Matsuo H., Iwata A., Horiba I., and Suzumura N.** (1993). Threedimensional image reconstruction by digital tomosynthesis using inverse filtering. *IEEE Trans Med Imag* 12: 307–313.
- [69] **Grant D. G.** (1972). Tomosynthesis: a three-dimensional radiographic imaging technique. *IEEE Trans Biomed Eng BME-* 19: 20–28.
- [70] **Chen Y., Lo J. Y., and Dobbins J. T. III.** (2007). Importance of point-by-point back projection (BP) correction for isocentric motion in digital breast tomosynthesis: Relevance to morphology of microcalcifications. *Med Phys* 34(10): 3885–3892.
- [71] **Bissonnette M., Hansroul M., Masson E., Savard S., Cadieux S., Warmoes P., Gravel D., Agopyan J., Polischuk B. T., Haerer W. H., Mertelmeier T., Lo J. Y., Chen Y., Dobbins J. T. III, Jesneck J. L., and Singh S.** (2005). Digital breast tomosynthesis using an amorphous selenium flat panel detector. *Proc SPIE* 5745: 529–540.
- [72] **Karellas A., Lo J. Y., and Orton C. G.** (2008). Point/Counterpoint. Cone beam x-ray CT will be superior to digital x-ray tomosynthesis in imaging the breast and delineating cancer. *Med Phys* 35(2): 409–411.
- [73] **Karellas A. and Vedantham S.** (2008). Breast cancer imaging: a perspective for the next decade. *Med Phys* 35(11): 4878–4897.

- [74] **Gong X. et al.** (2006). A computer simulation study comparing lesion detection accuracy with digital mammography, breast tomosynthesis, and cone-beam CT breast imaging. *Med Phys* 3(4): 1041–1052.
- [75] **Gordon R., Bender R., and Herman G. T.** (1970). Algebraic Reconstruction Techniques (ART) for Three-dimensional Electron Microscopy and X-ray Photography. *J. Theor. Biol.* 29, 471-481.
- [76] **Lent A.** (1977). A convergent algorithm for maximum entropy image restoration, with a medical x-ray application. *Image Analysis and Evaluation* ed R Shaw (Washington, DC: Society of Photographic Scientists and Engineers) pp 249–57
- [77] **Lent A. and Censor Y.** (1991). The primal-dual algorithm as a constraint-set-manipulation device. *Math. Program.* 50 343–57.
- [78] **Darroch J. N. and Ratcliff D.** (1972). Generalized iterative scaling for log-linear models. *Ann. Math. Stat.* 43 1470–80
- [79] **Meisters G. H. and Ulam S. M.** (1967). On visual hulls of sets. *Proc. Natl. Acad. Sci. USA.* 57 1172–4
- [80] **Beyer W. A. and Ulam S. M.** (1968). Note on the visual hull of a set. *J. Comb. Theory* 4 240–5
- [81] **Chaudhuri B. B. and Rosenfeld A.** (1998). On the computation of the digital convex hull and circular hull of a digital region. *Pattern Recognit.* 31 2007–16
- [82] **Herman, G. T. and Lent, A.** (1976). Iterative reconstruction algorithms. *Computers in Biology and Medicine*, 6:273-294.

CURRICULUM VITA



Candidate's full name: Kübra Cengiz

Place and date of birth: Manisa/Turkey-07.04.1989

Permanent Address: Istanbul/Turkey

Universities and Colleges attended:

- **MSc.:** Istanbul Technical University Department of Computer Engineering, Istanbul, Turkey
- **BA:** Yıldız Technical University Department of Computer Engineering, Istanbul, Turkey

Publications:

- Saeed Seyyedi, **Kubra Cengiz**, Mustafa Kamasak, and Isa Yildirim. "An Object-Oriented Simulator for 3D Digital Breast Tomosynthesis Imaging System", *Comp. and Math. Meth. in Med.*, Volume 2013 (2013), Article ID 250689 doi:10.1155/2013/250689.
- Saeed Seyyedi, **Kubra Cengiz**, Mustafa Kamasak, and Isa Yildirim. "An object-oriented simulator for 3D digital breast tomosynthesis system". 8th International Symposium on Image and Signal Processing and Analysis (ISPA 2013), Trieste, Italy, September 4-6 2013.
- Ertas M., Akan A. , **Cengiz K.**, Kamasak M., Seyyedi S., and Yildirim I., 2012: 3-D Tomosynthesis Image Reconstruction Using Total Variation. *International Conference on BioMedical Computing (BioMedCom 2012)*, Dec 14-16, 2012 Washington DC.